Journal of Science and Technology in Civil Engineering, HUCE, 2025, 19 (4): 29–45

STATIC BENDING AND BUCKLING ANALYSES OF GPL-FGM MICROPLATES PLACED ON WINKLER-PASTERNAK ELASTIC FOUNDATION

Jaroon Rungamornrat[a], Van-Loi Nguyen[b,*], Minh-Tu Tran[b]

[a]*Center of Excellence in Applied Mechanics and Structures & Center of Digital Asset Management for Sustainable Development, Department of Civil Engineering, Faculty of Engineering, Chulalongkorn University, Bangkok, 10330, Thailand*

[b]*Faculty of Building and Industrial Construction, Hanoi University of Civil Engineering, 55 Giai Phong road, Bach Mai ward, Hanoi, Vietnam*

Article history:
Received 03/11/2025, Revised 01/12/2025, Accepted 10/12/2025

Abstract

In this article, the static bending and buckling behaviors of microplates resting on a Winkler-Pasternak elastic foundation is studied. The microplate model is composed of metal-ceramic functionally graded material (FGM) reinforced by graphene nanoplatelets (GPLs), forming a GPL-FGM microplate. The FGM matrix properties vary according to the power-law distribution model, whereas the GPLs are distributed following five patterns (D1, D2, D3, D4 and D5) across the thickness. The governing equations for static bending and buckling analyses of the microplate model are derived utilizing the modified couple stress theory (MCST), four-unknown refined plate theory, and the Ritz method. The proposed solution is verified through comparison with existing results from the literature, and influence of some key factors on the non-dimensional deflection and the critical buckling load of the microplate are studied.

Keywords: static bending analysis; buckling analysis; GPL-reinforced FGM microplate; modified couple stress theory; four-unknown refined plate theory; Ritz method.

https://doi.org/10.31814/stce.huce2025-19(4)-03

---

1. Introduction

Nowadays, a wide range of industries, including electronics, automation, nano-electromechanical systems (NEMS), micro-electromechanical systems (MEMS), and more, use nano/microstructures [1, 2]. Microbeams/microplates are key components of various microdevices. Thus, a study on the mechanical behaviour of microstructures is necessary. In the past decade, functionally graded materials (FGMs) made of two constituent materials, metal and ceramic, have been a key research trend [3–5] because of their outstanding material properties, including high strength, high-temperature resistance, and corrosion resistance. To enhance the material properties, a FGM model reinforced by GPLs (GPL-FGM model) was introduced recently [6], promising a potential research direction [7, 8]. Since research on this model is quite limited, the present article will focus on studying a GPL-FGM microplate model.

To analyze nano-scale structures, the continuum mechanics–based theories that are commonly employed include the nonlocal elasticity theory [9, 10], the strain gradient theory [11, 12], the nonlocal strain gradient theory [13], etc. Currently, many studies on nanostructures have been reported, as summarized in the review article [14]. Recent research on nanostructures can also be found using isogeometric analysis [15–17] and the Ritz method [18]. For the analysis of micro-scale structures,

---

[*] Corresponding author. *E-mail address:* loinv@huce.edu.vn (Loi, N. V.)

the modified couple stress theory (MCST) and the modified strain gradient theory (MSGT) are the two most widely used size-dependent continuum theories in recent years. Among them, the MCST proposed by Yang et al. [19] has the advantage of employing only a single material length scale parameter while maintaining the accuracy of computational results. Based on the MCST, numerous analytical and numerical models for micro-structural analysis have been developed. For example, Xia et al. [20] performed nonlinear analyses of vibration, static bending, and post-buckling behaviour of microbeams, and their results demonstrated that the size-dependent effect must be considered since it has a significant impact on the mechanical response of microbeams. Reddy and Berry [21] provided a nonlinear theoretical formulation for the axisymmetric bending of circular FGM microplates using the MCST. Lien and Ha [22] also carried out a vibration analysis of functionally graded microbeams placed on a Winkler–Pasternak elastic foundation utilizing the Timoshenko beam theory, MCST, and the finite element method. Employing the isogeometric analysis (IGA) method, the first-order four-unknown plate theory, and MCST, Liu et al. [23] investigated the effects of size dependency on the static bending, buckling, and vibration behaviour of FGM microplates. It can be observed that most of the existing research studies in the literature have focused on FGM microbeams/microplates. The number of studies on micro-structures made of the GPL-FGM model are quite limited, only a few recent works addressing vibration and buckling behaviours [24, 25].

Semi-analytical methods like the Ritz-type solution, although requiring improvements in computational efficiency, have the advantage of not requiring mesh generation compared to numerical methods. In addition, the Ritz method is relatively flexible in handling various boundary conditions compared to analytical methods. Solutions for engineering structures using the Ritz method can provide benchmark solutions for validating other computational approaches. Recently, numerous studies have investigated the responses of various structures at the macro-, micro-, and nanoscale using Ritz-type solutions [26–28].

Based on the above-mentioned review, this study focuses on static bending and buckling analyses of a GPL-FGM microplate with the Winkler-Pasternak elastic foundation. Here, the modified couple stress theory, and the four-unknown refined plate theory, the Ritz method are used to derive the governing equations for such problems. In numerical investigations, the present results are first validated by other works in the existing literature. Then, the effect of some key factors (material parameters, boundary conditions, size-dependent effect, and foundation coefficients) on the deflection and the critical buckling load of the plate model is investigated.

2. Material model, kinetic relations, and energy expressions

2.1. GPL-FGM microplate

A microplate with a width a, a length b, and a thickness h, along x-, y- and z-directions, respectively, is considered (see, Fig. 1). Here, the microplate resting on Winkler-Pasternak elastic foundation subjected to a uniformly distributed transverse load and biaxial in-plane compression are illustrated in Fig. 1(a) and Fig. 1(b), respectively. The GPL-reinforced FGM microplate is assumed to have a metal-rich lower surface and a ceramic-rich upper surface.

For the FGM base, material properties, including elastic Young's modulus E_M, mass density ρ_M and Poisson's ratio ν_M are assumed to vary following the power-law pattern along the thickness as follows:

$$P_M(z) = (P_2 - P_1)\left(\frac{z}{h} + \frac{1}{2}\right)^p + P_1 \tag{1}$$

in which p is the power-law index, and P_1 and P_2 are material properties of the metal and ceramic constituents. The Young's modulus of the composite (i.e., GPL-FGM model) is estimated by the

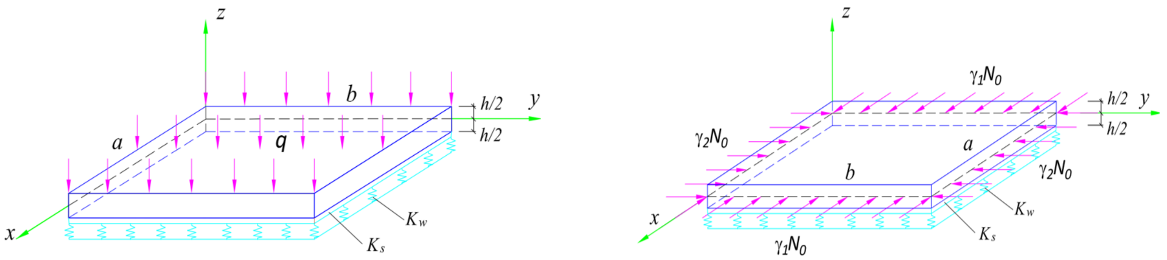

(a) Static bending analysis

(b) Buckling analysis

Figure 1. A GPL-FGM microplate resting on Winkler-Pasternak foundation model

modified Halpin-Tsai model as follows [29]:

$$E_c(z) = \left[\frac{3}{8}\frac{1+\hat{\xi}_{11}\hat{\eta}_{11}V_{GPL}(z)}{1-\hat{\eta}_{11}V_{GPL}(z)} + \frac{5}{8}\frac{1+\hat{\xi}_{22}\hat{\eta}_{22}V_{GPL}(z)}{1-\hat{\eta}_{22}V_{GPL}(z)}\right]E_M(z) \tag{2}$$

Notice that $V_{GPL}(z)$ is volume fraction of the GPLs; and parameters $(\hat{\xi}_{11}, \hat{\xi}_{22})$ and $(\hat{\eta}_{11}, \hat{\eta}_{22})$ are computed as follows:

$$\hat{\xi}_{11} = 2\left(l_{GPL}/t_{GPL}\right), \quad \hat{\xi}_{22} = 2\left(b_{GPL}/t_{GPL}\right) \tag{3}$$

$$\hat{\eta}_{11} = \frac{E_{GPL}-E_M}{E_{GPL}+\hat{\xi}_{11}E_M}, \quad \hat{\eta}_{22} = \frac{E_{GPL}-E_M}{E_{GPL}+\hat{\xi}_{22}E_M} \tag{4}$$

where E_{GPL}, l_{GPL}, b_{GPL}, and t_{GPL} represent the elastic modulus, average length, average width, and average thickness of the GPLs. The Poisson's ratio of the composite can be computed by [6]:

$$\nu_c(z) = \nu_{GPL}V_{GPL}(z) + \nu_M(z)\left[1 - V_{GPL}(z)\right] \tag{5}$$

in which ν_{GPL} is the Poisson's ratio of the GPLs. In this study, the distribution of GPLs in the plate model is assumed to be approximately continuous through the thickness and follows five variation patterns: symmetric D1, symmetric D2, asymmetric D3, asymmetric D4, and uniform D5, as illustrated in Fig. 2. The GPL volume fraction $V_{GPL}(z)$ of each pattern is determined as follows [30]:

$$V_{GPL}(z) = \left\{V_1 d_1(z), V_2 d_2(z), V_3 d_3(z), V_4 d_4(z), V_5 d_5(z)\right\} \tag{6}$$

where

$$\begin{cases} d_1(z) = 1-\cos\left(\dfrac{\pi z}{h}\right), d_2(z) = \cos\left(\dfrac{\pi z}{h}\right), d_3(z) = 1-\cos\left(\dfrac{\pi z}{2h}+\dfrac{\pi}{4}\right), \\ d_4(z) = 1-\sin\left(\dfrac{\pi z}{2h}+\dfrac{\pi}{4}\right), d_5(z) = 1 \end{cases} \tag{7}$$

In Eq. (6), value of V_i $(i = 1,2,3,4,5)$ of pattern D_i, can be computed by [6]:

$$V_i = \frac{W_{GPL}a}{W_{GPL}c_i + \rho_{GPL}\left(1-W_{GPL}\right)b_i}, \quad (i = 1,2,3,4,5) \tag{8}$$

with

$$a = \int_{-\frac{h}{2}}^{\frac{h}{2}} \rho_M(z)\,dz, \quad b_i = \int_{-\frac{h}{2}}^{\frac{h}{2}} d_i(z)\,dz, \quad c_i = \int_{-\frac{h}{2}}^{\frac{h}{2}} \rho_M(z)\,d_i(z)\,dz \tag{9}$$

Note that W_{GPL} is total GPL weight fraction, defined as the ratio of the total GPL weight to the total weight of the composite.

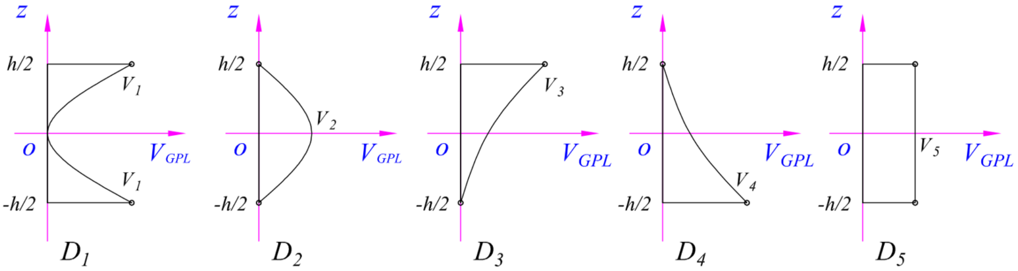

Figure 2. Five patterns of the GPL distribution along the microplate thickness

The determination of the effective material properties of the GPL-FGM model can be summarized in four steps as follows: (i) Input the required parameters such as the material properties of the ceramic, metal, and GPL; the power-law index p; the dimensions of the GPL; the total GPL weight fraction W_{GPL}; the GPL pattern; and the plate thickness. (ii) Use formulas (1), (3), and then (4) to calculate the material and GPL dimension parameters. (iii) For each GPL pattern, substitute formula (7) into (9), then substitute the obtained result into Eq. (8) and subsequently into Eq. (6) to determine the GPL volume fraction $V_{GPL}(z)$ corresponding to the pattern D_i. (iv) Finally, Young's modulus $E_c(z)$ and Poisson's ratio $\nu_c(z)$ of the composite can be computed using formulas (2) and (5).

2.2. Kinetic relations

Based on the four-unknown refined plate theory, the displacement components of the GPL-FGM microplate are defined as follows [31]:

$$\begin{aligned} u(x,y,z) &= u_0 - z w_{b,x} - f(z)\, w_{s,x} \\ v(x,y,z) &= v_0 - z w_{b,y} - f(z)\, w_{s,y} \\ w(x,y,z) &= w_b + w_s \end{aligned} \tag{10}$$

where u, v and w present the displacements of a certain point of the plate in the x-, y-, and z-directions, respectively. Corresponding displacement components on the midplane in x- and y-directions are denoted by letters u_0 and v_0. The bending and shear components of the total deflection w are denoted by letters w_b and w_s. In this paper, function $f(z) = -\frac{z}{8} + \frac{3}{2}\left(\frac{z^3}{h^2}\right)$ is chosen for analysis [31]. The strain-displacement relations of the plate model are determined by:

$$\begin{Bmatrix} \varepsilon_{xx} \\ \varepsilon_{yy} \\ \gamma_{xy} \end{Bmatrix} = \begin{Bmatrix} \varepsilon^0_{xx} \\ \varepsilon^0_{yy} \\ \gamma^0_{xy} \end{Bmatrix} + z \begin{Bmatrix} k^b_{xx} \\ k^b_{yy} \\ k^b_{xy} \end{Bmatrix} + f(z) \begin{Bmatrix} k^s_{xx} \\ k^s_{yy} \\ k^s_{xy} \end{Bmatrix}, \quad \begin{Bmatrix} \gamma_{yz} \\ \gamma_{xz} \end{Bmatrix} = g(z) \begin{Bmatrix} \gamma^0_{yz} \\ \gamma^0_{xz} \end{Bmatrix} \tag{11}$$

where

$$\begin{Bmatrix} \varepsilon^0_{xx} \\ \varepsilon^0_{yy} \\ \gamma^0_{xy} \end{Bmatrix} = \begin{Bmatrix} u_{0,x} \\ v_{0,y} \\ u_{0,y} + v_{0,x} \end{Bmatrix}, \quad \begin{Bmatrix} k^b_{xx} \\ k^b_{yy} \\ k^b_{xy} \end{Bmatrix} = \begin{Bmatrix} -w_{b,xx} \\ -w_{b,yy} \\ -2w_{b,xy} \end{Bmatrix}, \quad \begin{Bmatrix} k^s_{xx} \\ k^s_{yy} \\ k^s_{xy} \end{Bmatrix} = \begin{Bmatrix} -w_{s,xx} \\ -w_{s,yy} \\ -2w_{s,xy} \end{Bmatrix} \tag{12}$$

$$\begin{Bmatrix} \gamma^s_{yz} \\ \gamma^s_{xz} \end{Bmatrix} = \begin{Bmatrix} w_{s,y} \\ w_{s,x} \end{Bmatrix}, \quad g(z) = 1 - f'(z) \tag{13}$$

Based upon the MCST, the components of the curvature tensor of the microplate model are determined by [25]:

$$\begin{Bmatrix} \chi_{xx} \\ \chi_{yy} \\ \chi_{xy} \end{Bmatrix} = \begin{Bmatrix} \chi^0_{xx} \\ \chi^0_{yy} \\ \chi^0_{xy} \end{Bmatrix} + (1 + f_{,z}) \begin{Bmatrix} \chi^1_{xx} \\ \chi^1_{yy} \\ \chi^1_{xy} \end{Bmatrix}, \quad \begin{Bmatrix} \chi_{yz} \\ \chi_{xz} \end{Bmatrix} = \begin{Bmatrix} \chi^0_{yz} \\ \chi^0_{xz} \end{Bmatrix} + f_{,zz} \begin{Bmatrix} \chi^1_{yz} \\ \chi^1_{xz} \end{Bmatrix}, \quad \chi_{zz} = 0 \tag{14}$$

in which

$$\chi^0_{xx} = w_{b,xy}, \quad \chi^1_{xx} = \frac{1}{2} w_{s,xy}, \quad \chi^0_{yy} = -w_{b,xy}, \quad \chi^1_{yy} = -\frac{1}{2} w_{s,xy} \tag{15}$$

$$\chi^0_{xy} = \frac{1}{2}\left(w_{b,yy} - w_{b,xx}\right), \quad \chi^1_{xy} = \frac{1}{4}\left(w_{s,yy} - w_{s,xx}\right) \tag{16}$$

$$\chi^0_{yz} = \frac{1}{4}\left(v_{0,xy} - u_{0,yy}\right), \quad \chi^1_{yz} = -\frac{1}{4} w_{s,x}, \quad \chi^0_{xz} = \frac{1}{4}\left(v_{0,xx} - u_{0,xy}\right), \quad \chi^1_{xz} = \frac{1}{4} w_{s,y} \tag{17}$$

The stress-strain relationships of the microplate model are given by [32]:

$$\begin{Bmatrix} \sigma_{xx} \\ \sigma_{yy} \\ \sigma_{xy} \\ \sigma_{yz} \\ \sigma_{xz} \end{Bmatrix} = \begin{bmatrix} \bar{C}_{11} & \bar{C}_{12} & 0 & 0 & 0 \\ \bar{C}_{12} & \bar{C}_{22} & 0 & 0 & 0 \\ 0 & 0 & \bar{C}_{66} & 0 & 0 \\ 0 & 0 & 0 & \bar{C}_{44} & 0 \\ 0 & 0 & 0 & 0 & \bar{C}_{55} \end{bmatrix} \begin{Bmatrix} \varepsilon_{xx} \\ \varepsilon_{yy} \\ \gamma_{xy} \\ \gamma_{yz} \\ \gamma_{xz} \end{Bmatrix} \tag{18}$$

$$\left(t_{xx}, t_{yy}, t_{xy}, t_{yz}, t_{xz}\right) = 2G_c l_0^2 \left(\chi_{xx}, \chi_{yy}, \chi_{xy}, \chi_{yz}, \chi_{xz}\right) \tag{19}$$

where l_0 is the material length scale parameter, which characterizes the intrinsic microstructural effects of the material, and non-zero coefficients $\bar{C}_{ij}$ and G_c are computed by:

$$\begin{aligned} &\bar{C}_{11} = \bar{C}_{22} = \frac{E_c(z)}{1 - \nu_c^2(z)}, \quad \bar{C}_{12} = \frac{\nu_c(z) E_c(z)}{1 - \nu_c^2(z)} \\ &\bar{C}_{66} = \bar{C}_{44} = \bar{C}_{55} = G_c = E_c(z)/2/\left(1 + \nu_c(z)\right) \end{aligned} \tag{20}$$

Note that the stress resultants $(N_{xx}, N_{yy}, N_{xy}, M^b_{xx}, M^b_{yy}, M^b_{xy}, M^s_{xx}, M^s_{yy}, M^s_{xy}, Q_{xz}, Q_{yz})$ and $(P_{xx}, P_{yy}, P_{xy}, P_{yz}, P_{xz}, R_{xx}, R_{yy}, R_{xy}, S_{yz}, S_{xz})$ of the microplate are provided in detail in Appendix A.

2.3. *Energy expressions*

To derive the governing equation, energy expressions including the strain energy (U) of the plate, the strain energy of the elastic foundation (U_F), and potential energy (V) of external applied loads should be determined. The strain energy of the GPL-FGM microplate model is determined as follows:

$$U = \frac{1}{2} \int_A \begin{pmatrix} N_{xx}\varepsilon^0_{xx} + N_{yy}\varepsilon^0_{yy} + N_{xy}\gamma^0_{xy} + M^b_{xx}k^b_{xx} + M^b_{yy}k^b_{yy} + M^b_{xy}k^b_{xy} \\ +M^s_{xx}k^s_{xx} + M^s_{yy}k^s_{yy} + M^s_{xy}k^s_{xy} + Q_{yz}\gamma^s_{yz} + Q_{xz}\gamma^s_{xz} \\ +P_{xx}\chi^0_{xx} + P_{yy}\chi^0_{yy} + 2P_{xy}\chi^0_{xy} + 2P_{yz}\chi^0_{yz} + 2P_{xz}\chi^0_{xz} \\ +R_{xx}\chi^1_{xx} + R_{yy}\chi^1_{yy} + 2R_{xy}\chi^1_{xy} + 2S_{yz}\chi^1_{yz} + 2S_{xz}\chi^1_{xz} \end{pmatrix} dA \tag{21}$$

The strain energy expression of the elastic foundation is determined by

$$U_F = \frac{1}{2} \int_A \left\{ K_w w^2 + K_s \left[\left(w_{,x}\right)^2 + \left(w_{,y}\right)^2 \right] \right\} dA \tag{22}$$

In this context, the Winkler foundation stiffness K_w and Pasternak shear stiffness K_s represent the vertical elastic resistance and the shear transfer capability (shear interaction) of the elastic foundation, respectively. The potential energy of external applied loads can be determined by [33]:

$$V = -\int_A qwdA - \frac{1}{2}\int_A \left[N_{x0}(w_{,x})^2 + N_{y0}\left(w_{,y}\right)^2 + 2N_{xy0}w_{,x}w_{,y}\right]dA \tag{23}$$

in which q is distributed transverse load, and N_{x0}, N_{y0} and N_{xy0} are in-plane normal and shear loadings. The total energy functional $\hat{\Pi}$ of the microplate model can be defined by:

$$\hat{\Pi} = U + U_F + V \tag{24}$$

3. Solution procedure

Consider a rectangular GPL-FGM microplate placed on a Winkler–Pasternak elastic foundation as illustrated in Fig. 1. The adopted plate is subjected to a uniformly distributed transverse load $q = q_0$ and to in-plane compressive loads in the mid-plane in two directions given by $N_{x0} = \gamma_1 N_0, N_{y0} = \gamma_2 N_0, N_{xy0} = 0$. For convenience, the following coordinate transformation is used in the present study:

$$\xi = \frac{2x}{a} - 1, \quad \eta = \frac{2y}{b} - 1 \tag{25}$$

Based on the pb-2 Ritz functions, the components of the displacement field of the microplate are expanded in the following form [34]:

$$\begin{aligned}
u_0(x,y,t) &= \sum_{s=0}^{N^*}\sum_{r=0}^{s} T_{sr}u_{sr}(\xi,\eta) = \sum_{j=1}^{M} T_j u_j(\xi,\eta)\\
v_0(x,y,t) &= \sum_{s=0}^{N^*}\sum_{r=0}^{s} H_{sr}v_{sr}(\xi,\eta) = \sum_{j=1}^{M} H_j v_j(\xi,\eta)\\
w_b(x,y,t) &= \sum_{s=0}^{N^*}\sum_{r=0}^{s} X_{sr}w_{bsr}(\xi,\eta) = \sum_{j=1}^{M} X_j w_{bj}(\xi,\eta)\\
w_s(x,y,t) &= \sum_{s=0}^{N^*}\sum_{r=0}^{s} Y_{sr}w_{ssr}(\xi,\eta) = \sum_{j=1}^{M} Y_j w_{sj}(\xi,\eta)
\end{aligned} \tag{26}$$

Here, N^* denotes the order of the 2D polynomial. The quantities (T_j, H_j, X_j, Y_j) are the coefficients need be determined. The number of terms M and the index j of the series in Eq. (26) are defined by:

$$M = \frac{(N^*+1)(N^*+2)}{2}, \quad j = \frac{(s+1)(s+2)}{2} - (s-r) \tag{27}$$

The Ritz functions $\left(u_j, v_j, w_{bj}, w_{sj}\right)$ in Eq. (26) for different boundary conditions are provided similarly in [34, 35]. Note that the "C" and "S" stands for clamped and simply supported boundary conditions at each edge of the microplate. In this study, plates with CCCC (fully clamped), SSSS (fully simply supported), and SCSC (two opposite sides having the same boundary conditions) boundary conditions are considered in numerical investigations.

The displacement field (26) is substituted into the total energy functional (24), and the Lagrange equation is applied as follows:

$$\frac{\partial \hat{\Pi}}{\partial p_j} = 0, \quad j = 1, 2, \ldots, M \tag{28}$$

where p_j represents the coefficients $\left(T_j, H_j, X_j, Y_j\right)$. Finally, the governing equation of the problem can be achieved as follows:

$$\left(\mathbf{K} - N_0 \mathbf{K}_g\right) \mathbf{Q} = \mathbf{F} \tag{29}$$

where $\mathbf{K}$ and $\mathbf{K}_g$ denote the elastic stiffness and the geometric stiffness matrices, respectively; $\mathbf{Q}$ is the vector of displacement coefficients; $\mathbf{F}$ is the load vector; and N_0 represents the buckling load of the plate model.

For the static bending problem, the following governing equation is obtained:

$$\mathbf{KQ} = \mathbf{F} \tag{30}$$

By solving Eq. (30), the vector of displacement coefficients ($\mathbf{Q}$) can be computed; then displacement, strain, and stress components within the microplate can be achieved.

For the buckling problem, the governing equation are the following:

$$\left(\mathbf{K} - N_0 \mathbf{K}_g\right) \mathbf{Q} = \mathbf{0} \tag{31}$$

The buckling load N_0 of the microplate can be obtained by solving Eq. (31). The critical buckling load (N_{cr}) corresponds to the smallest value among these buckling loads.

4. Verification examples

In the numerical analyses, the microplate made from Al/ZrO$_2$, the material properties of metal (Al) and ceramic (ZrO$_2$) as $E_1 = 70$ GPa, $\nu_1 = 0.3, \rho_1 = 2702$ kg/m^3 and $E_2 = 151$ GPa, $\nu_2 = 0.3, \rho_2 = 3000$ kg/m^3, respectively. The parameters of the GPL are used as $E_{GPL} = 1010$ GPa, $\rho_{GPL} = 1062.5$ kg/m^3, $\nu_{GPL} = 0.186$, $l_{GPL} = 3$ nm, $b_{GPL} = 1.8$ nm, and $t_{GPL} = 0.7$ nm [36]. Since no experimental data are available for GPL-FGM model, the material length scale parameter is taken approximately as $l_0 = 17.6$ µm [32]. For convenience, the following non-dimensional quantities are used in this study [32, 37]:

$$\bar{w} = \frac{10E_2h^3}{q_0a^4} w\left(\frac{a}{2}, \frac{b}{2}\right); \; \bar{N} = \frac{N_{cr}a^2}{E_1h^3}; \; \bar{K}_0 = \frac{K_wa^4}{D_m}; \; \bar{J}_0 = \frac{K_sa^2}{D_m}; \; D_m = \frac{E_1h^3}{12(1-\nu_1^2)} \tag{32}$$

4.1. Convergence study

In this subsection, the convergence of the non-dimensional critical buckling load $\bar{N}$ and non-dimensional deflection $\bar{w}$ of the GPL-FGM microplate placed on an elastic foundation is presented, where the degree of the polynomial (N^*) of the series is increased from 1 to 10. The GPL-FGM microplate with the SSSS boundary and input parameters as $b/a = 1$, $\bar{K}_0 = 50$, $\bar{J}_0 = 50$, $p = 1$ and GPL reinforcement following the symmetric distribution D1 with GPL weight fraction as $W_{GPL} = 1.5\%$ for the convergence study are considered. Notice that the deflection $\bar{w}$ of the GPL-FGM microplate under a uniformly distributed transverse load q_0 is listed in Table 1, while the critical load $\bar{N}$ of the microplate under a biaxial compression ($\gamma_1 = 1$, $\gamma_2 = 1$) is shown in Table 2. It can be seen that the quantities $\bar{w}$ and $\bar{N}$ of the GPL-FGM microplate converge when $N^* \geq 8$ as shown in the Tables. To maintain the stability and reliability of the numerical results, $N^* = 10$ is adopted for all subsequent numerical analyses.

Table 1. Convergence study of central deflection $\bar{w}$ of the GPL-FGM microplate

a/h	l_0/h	N^*							
		1	3	5	6	7	8	9	10
5	0	0.2154	0.2196	0.2183	0.2184	0.2184	0.2183	0.2183	0.2184
	0.5	0.1464	0.1564	0.1546	0.1549	0.1549	0.1548	0.1548	0.1548
	1	0.0749	0.0828	0.0820	0.0821	0.0821	0.0821	0.0821	0.0821
30	0	0.1952	0.2083	0.2050	0.2053	0.2053	0.2052	0.2052	0.2052
	0.5	0.1349	0.1477	0.1458	0.1460	0.1460	0.1459	0.1459	0.1459
	1	0.0700	0.0786	0.0778	0.0779	0.0779	0.0779	0.0779	0.0779
200	0	0.1945	0.2079	0.2046	0.2049	0.2049	0.2048	0.2048	0.2048
	0.5	0.1346	0.1474	0.1456	0.1457	0.1457	0.1457	0.1457	0.1457
	1	0.0699	0.0785	0.0777	0.0778	0.0778	0.0778	0.0778	0.0778

Table 2. Convergence study of critical load $\bar{N}$ of the GPL-FGM microplate

a/h	l_0/h	N^*							
		1	3	5	6	7	8	9	10
5	0	7.823	7.579	7.578	7.578	7.578	7.578	7.578	7.578
	0.5	11.514	10.910	10.907	10.907	10.907	10.907	10.907	10.907
	1	22.497	20.824	20.817	20.817	20.817	20.817	20.817	20.817
30	0	8.634	8.248	8.246	8.246	8.246	8.246	8.246	8.246
	0.5	12.492	11.712	11.709	11.709	11.709	11.709	11.709	11.709
	1	24.062	22.100	22.091	22.091	22.091	22.091	22.091	22.091
200	0	8.663	8.271	8.270	8.270	8.270	8.270	8.270	8.270
	0.5	12.525	11.739	11.735	11.735	11.735	11.735	11.735	11.735
	1	24.112	22.140	22.131	22.131	22.131	22.131	22.131	22.131

4.2. Static bending of FGM microplate

In this example, the non-dimensional central deflections, $\tilde{w} = \dfrac{100E_1h^3}{q_0a^4}w\left(\dfrac{a}{2},\dfrac{b}{2}\right)$, of FGM microplate under a uniformly distributed transverse load q_0 are validated against the results reported by Abazid and Sobhy [38]. The FGM microplate considered here has simply supported edges (SSSS) and an aspect ratio $b/a = 1$. Comparisons are made for various thickness ratios a/h, and power-law indices p, as presented in Table 3. Note that the input parameters are taken as in Ref. [38]. It can be seen that the discrepancies between the present plate model and those of Abazid and Sobhy [38], which employed the four-unknown refined plate theory and the Navier solution, are insignificant. The differences between the two models arise because Abazid and Sobhy [38] used a different form of the function $f(z)$ in the displacement field compared to that of the present study.

Table 3. The central deflection $\tilde{w}$ of the FGM microplate

a/h	l_0/h	Source	p		
			0	1	10
20	0	Abazid and Sobhy [38]	0.4229	0.9867	2.1369
		Present	0.4232	0.9873	2.1371
		Diff. (%)	0.07	0.06	0.01
	1	Abazid and Sobhy [38]	0.0887	0.1693	0.4779
		Present	0.0889	0.1695	0.4776
		Diff. (%)	0.23	0.12	0.06
5	0	Abazid and Sobhy [38]	0.5095	1.1441	2.8261
		Present	0.5145	1.1533	2.8337
		Diff. (%)	0.98	0.80	0.27
	1	Abazid and Sobhy [38]	0.0942	0.1784	0.5026
		Present	0.0963	0.1816	0.4986
		Diff. (%)	2.23	1.79	0.80

4.3. Buckling of FGM microplate with elastic foundations

In this example, the non-dimensional critical loads, $\bar{N} = N_{cr}a^2/(E_1h^3)$, of FGM microplate placed on a Winkler-Pasternak foundation, subjected to bi-axial compression ($\gamma_1 = 1, \gamma_2 = 1$), are compared with those of Van Hieu et al. [39], as listed in Table 4. The elastic foundation parameters $(\hat{K}_w, \hat{K}_s)$ and input data of the problem are taken as in Ref. [39]. It can be observed the discrepancies between results of the present model and those of Van Hieu et al. [39] using the Mindlin plate model and Navier-type solution is very insignificant ($l_0/h = 0.2$). The differences here arise from the fact that the two models are based on different plate theories.

Table 4. The critical load $\bar{N}$ of the FGM microplate placed on the Winkler-Pasternak foundation ($l_0/h = 0.2$)

$(\hat{K}_w, \hat{K}_s)$	(0,10)	(10,10)	(15,10)	(20,10)	(25,10)	(30,10)
Van Hieu et al. [39]	52.038	54.460	55.671	56.882	58.093	59.305
Present	52.028	54.451	55.662	56.873	58.084	59.295
Diff. (%)	0.02	0.02	0.02	0.02	0.02	0.02

4.4. Buckling of GPL-reinforced macroplate

To verify the GPL-reinforced plate, the non-dimensional critical buckling loads, $\tilde{N} = \left(1 - \nu_1^2\right) N_{cr}/\left(E_1 h\right)$, of the GPL-reinforced isotropic plate under uniaxial compression ($\gamma_1 = 0, \gamma_2 = 1$) are compared with those of Nguyen and Pham [40]. The comparison results between the two models are listed in Table 5. We can see that the present results agree well with those of Nguyen and Pham [40] using isogeometric analysis (IGA) in SSSS and CCCC boundary cases. It can be noted that the two models employed the same four-unknown refined plate theory. The slight differences observed are because the two models are based on different computational methods (i.e., the Ritz and IGA methods).

From the above verification cases, it can be seen that the theoretical model and the solutions presented in this article are highly reliable. Thus, it can be used to investigate the influence of material properties, the size-dependent effect, boundary conditions, and elastic foundation parameters on the non-dimensional deflection and critical buckling load of the GPL-FGM microplate model in the next parametric studies.

Table 5. The non-dimensional critical load $\tilde{N}$ of the GPL-reinforced plate

Boundary conditions	Source	W_{GPL} (%)			
		0	0.1	0.5	1
SSSS	Nguyen and Pham [40]	0.0310	0.0413	0.0825	0.1340
	Present	0.0310	0.0413	0.0825	0.1340
	Diff. (%)	0.00	0.00	0.00	0.00
CCCC	Nguyen and Pham [40]	0.0692	0.0922	0.1841	0.2989
	Present	0.0691	0.0921	0.1839	0.2985
	Diff. (%)	0.14	0.11	0.11	0.13

5. Parametric study

In the next numerical investigations, the FGM plate model made of Al/ZrO$_2$ reinforced by GPLs is studied. The purpose of parametric study is to investigate the underlying mechanical trends of GPL-FGM microplates under representative loading and boundary conditions; thus, the input parameters used in the analysis are defined as the following:

- A rectangular microplate with SSSS boundary condition and geometric ratios $b/a = 1$, $a/h = 30$, $h/l_0 = 1$, $l_0 = 17.6 \times 10^{-6}$ m is considered.

- The FGM base material has a power-law index of $p = 1$, and the GPL distribution follows the pattern D1 (symmetric) with a GPL weight fraction $W_{GPL} = 1.5\%$.

- Elastic foundation parameters: $\bar{K}_0 = \bar{J}_0 = 0$ ($K_w = 0$ N/m^3, $K_s = 0$ N/m^2).

- In the static bending problem, the microplate under to a uniformly distributed transverse load $q = q_0 = 10^4$ N/m^2 is studied.

- In the buckling problem, the microplate is under uniform biaxial compressive loads characterized by the parameters $\gamma_1 = 1, \gamma_2 = 1$ ($N_{x0} = N_{y0} = N_0$ (N/m)).

5.1. Influence of size-dependent effect and power-law index

The influence of the size-dependent effect (represented by the ratio h/l_0) and the power-law index (p) on the non-dimensional critical buckling load $\bar{N}$ and the non-dimensional central deflection $\bar{w}$ of the SSSS GPL-FGM microplate are illustrated in Fig. 3. In this example, the ratio h/l_0 varies from 1 to 20, while the index p changes from 0 to 10. The results for the cases of the GPL-FGM microplate under uniaxial and biaxial compressions are presented in Fig. 3(a) and Fig. 3(b), respectively, whereas the non-dimensional deflection $\bar{w}$ of the GPL-FGM microplate under uniformly distributed transverse load is plotted in Fig. 3(c).

It is evident that as the ratio h/l_0 decreases (i.e., as the plate size becomes smaller), the critical load $\bar{N}$ of the microplate increases sharply both uniaxial and biaxial compressions, as shown in Fig. 3(a) and Fig. 3(b). In contrast, the non-dimensional deflection $\bar{w}$ decreases significantly, indicating an increase in the plate stiffness, as illustrated in Fig. 3(c). At this range, the influence of the size-dependent effect on the mechanical response of the GPL-FGM microplate becomes more substantial. However, when the ratio $h/l_0 > 10$, both the critical buckling load $\bar{N}$ and the deflection $\bar{w}$ of the microplate exhibit negligible change, and their values tend to approach those of a macro-scale plate. For example, when $W_{GPL} = 1.5\%$ with the pattern D1, and for $p = 1$, the critical load $\bar{N}$ of the microplate under biaxial compression increases from 3.4701 at $h/l_0 = 20$ to 17.2807 at $h/l_0 = 1$, corresponding to an increase of 397.99% (as shown in Fig. 3(b)). Similarly, the deflection $\bar{w}$ of the microplate reduces from 0.4982 at $h/l_0 = 20$ to 0.1001 at $h/l_0 = 1$, corresponding to a decrease of 79.91% (as shown in Fig. 3(c)). Furthermore, when the power-law index p increases (corresponding to a decrease in ceramic content), the critical load $\bar{N}$ decreases while the deflection $\bar{w}$ of the plate increases. This behaviour results from the reduction in plate stiffness due to the decreased proportion of the stiffer ceramic content within the FGM microplate.

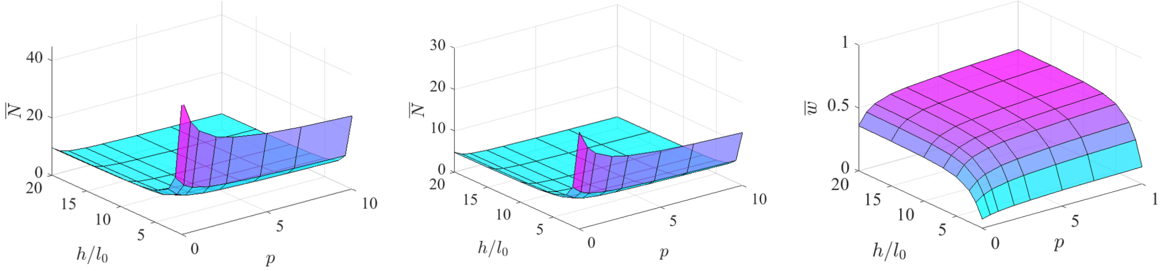

(a) Critical load (Uniaxial compression)

(b) Critical load (Biaxial compression)

(c) Deflection

Figure 3. Variation of critical load $\bar{N}$ and deflection $\bar{w}$ with respect to h/l_0 and p ($b/a = 1$, $a/h = 30$, $W_{GPL} = 1.5\%$, $\bar{K}_0 = \bar{J}_0 = 0$, $\gamma_1 = 1, \gamma_2 = 1$, $q = q_0$)

5.2. *Influence of GPL patterns and weight fraction*

In this subsection, the effect of the distribution patterns and the weight fraction of GPLs (W_{GPL}) on the critical load $\bar{N}$ and the deflection $\bar{w}$ of the SSSS GPL-FGM microplate with the SSSS boundary condition are presented. Specifically, by varying the GPL weight fraction W_{GPL} from 0% to 3%, the critical load $\bar{N}$ for the microplate under uniform uniaxial and biaxial compressions are illustrated in Fig. 4(a) and Fig. 4(b), respectively, while the deflection $\bar{w}$ of the GPL-FGM microplate subjected to a uniformly distributed transverse load is shown in Fig. 4(c). In this analysis, five GPL distribution patterns—D1, D2, D3, D4, and D5—are considered.

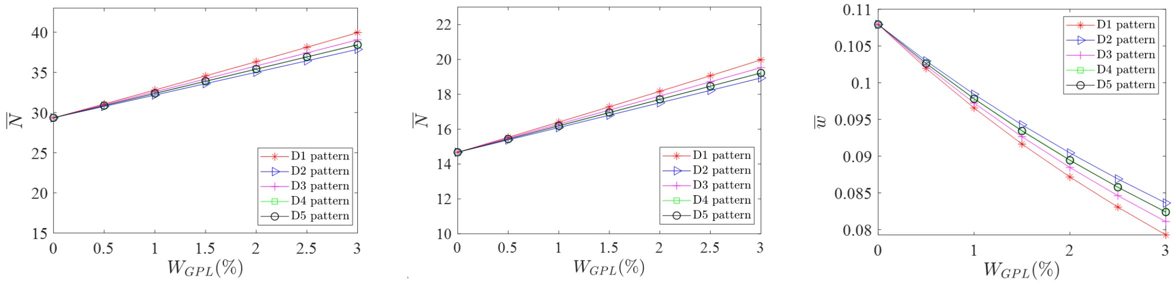

(a) Critical load (Uniaxial compression)

(b) Critical load (Biaxial compression)

(c) Deflection

Figure 4. Variation of critical load $\bar{N}$ and deflection $\bar{w}$ with respect to W_{GPL} ($b/a = 1$, $a/h = 30$, $p = 1$, $h/l_0 = 1$, $\bar{K}_0 = \bar{J}_0 = 0$, $\gamma_1 = 1, \gamma_2 = 1$, $q = q_0$)

It is evident that the critical buckling load $\bar{N}$ of the GPL-FGM microplate rises steadily, while the central deflection $\bar{w}$ decreases significantly as the GPL weight fraction increases. This trend is consistent across all five GPL patterns, as illustrated in Fig. 4. Moreover, the microplate with the pattern D1 (symmetric) exhibits the highest non-dimensional critical load ($\bar{N}$) and the lowest non-dimensional central deflection ($\bar{w}$), indicating the most effective reinforcement performance. In contrast, the microplate with the D2 pattern shows the lowest non-dimensional critical load and the largest non-dimensional central deflection. It is clear that when the deformation or buckling mode of the plate model is dominated by transverse displacement (z-direction), the pattern D1 provides the most efficient GPL reinforcement among the five patterns investigated. Furthermore, the GPL reinforcement significantly enhances the critical load $\bar{N}$ and reduces the central deflection $\bar{w}$ of the GPL-FGM microplate. For instance, when $W_{GPL} = 1.5\%$ with the distribution pattern D1, the critical load $\bar{N}$ of the microplate with the SSSS boundary increases by approximately 17.8%, while its deflection $\bar{w}$ decreases by about 15.1% compared with the case without GPLs. When $W_{GPL} = 3\%$, the critical load $\bar{N}$ increases by approximately 36.1%, and the deflection $\bar{w}$ decreases by about 26.5%, again compared with the case without GPLs.

5.3. *Influence of various boundary conditions*

In this investigation, the influence of different boundary conditions on the critical load $\bar{N}$ and the central deflection $\bar{w}$ of the GPL-FGM microplate with D1 pattern are presented. Here, the critical buckling load $\bar{N}$ and deflection $\bar{w}$ of the microplate subjected to various boundary conditions, including SSSS, SCSC, and CCCC, are evaluated. Note that results for the microplate model under biaxial compression are illustrated in Fig. 5(a), while the deflection $\bar{w}$ of the GPL-FGM microplate is presented in Fig. 5(b).

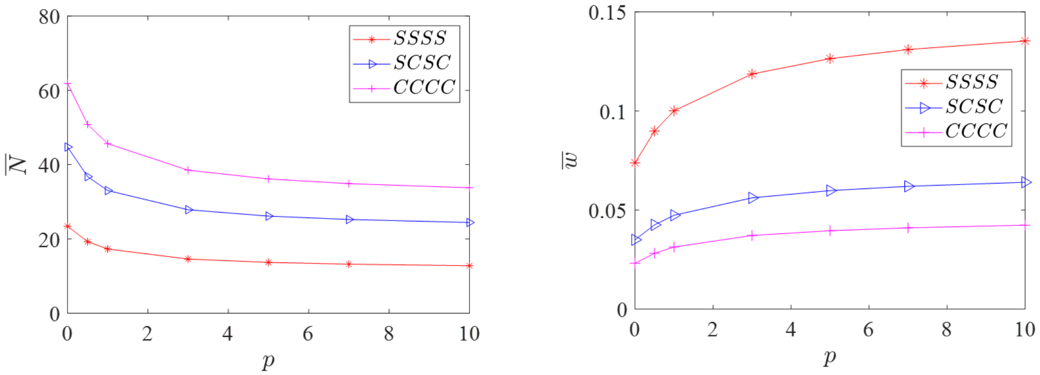

(a) Critical load (Biaxial compression)

(b) Deflection

Figure 5. Variation of the critical load $\bar{N}$ and deflection $\bar{w}$ with various boundary conditions ($b/a = 1, a/h = 30, h/l_0 = 1, W_{GPL} = 1.5\%, \bar{K}_0 = \bar{J}_0 = 0, \gamma_1 = 1, \gamma_2 = 1, q = q_0$)

From the graphs, it is clearly observed that when the power-law index (p) increases (corresponding to a decrease in ceramic content, hence a reduction in plate stiffness), the critical load $\bar{N}$ decreases, while the central deflection $\bar{w}$ of the microplate increases under all three boundary conditions. For example, when $W_{GPL} = 1.5\%$ with the pattern D1, and under the SSSS boundary, the critical load $\bar{N}$ of the microplate under biaxial compression decreases from 23.4182 at $p = 0$ to 12.7782 at $p = 10$, corresponding to a reduction of 45.43%. Similarly, the deflection $\bar{w}$ of the microplate increases from 0.0738 at $p = 0$ to 0.1353 at $p = 10$, corresponding to an increase of 83.3%. It can also be seen that the GPL-FGM microplate model with the CCCC boundary condition exhibits the highest critical load $\bar{N}$ and the smallest deflection $\bar{w}$, whereas the microplate with the SSSS boundary shows the lowest critical load $\bar{N}$ and the largest deflection $\bar{w}$ among the cases considered. This is because, in comparison to the other boundary types, the CCCC boundary condition significantly increases the microplate's stiffness. For example, when $W_{GPL} = 1.5\%$ with the pattern D1, and for $p = 1$, the critical load $\bar{N}$ of the microplate under biaxial compression increases from 17.2807 for the SSSS boundary to 45.6488 for the CCCC boundary, corresponding to an increase of 164.16%. Likewise, the deflection $\bar{w}$ of the microplate decreases from 0.1001 for the SSSS boundary to 0.0313 for the CCCC boundary, corresponding to a reduction of 68.73%. It is therefore evident that both the boundary conditions and the power-law index p have a pronounced influence on the critical load $\bar{N}$ and the central deflection $\bar{w}$ of the GPL-FGM microplate.

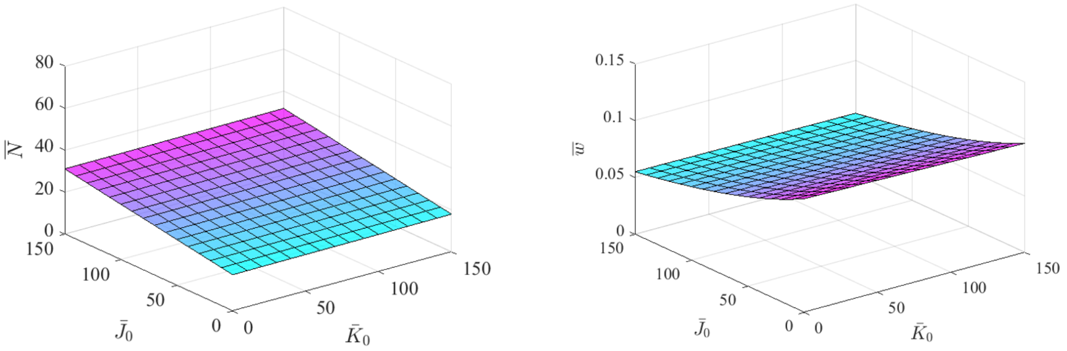

(a) Critical load (Biaxial compression)

(b) Deflection

Figure 6. Variation of critical load $\bar{N}$ and deflection $\bar{w}$ with respect to parameters $\bar{K}_0$, $\bar{J}_0$ ($b/a = 1$, $a/h = 30$, $p = 1$, $h/l_0 = 1$, $W_{GPL} = 1.5\%$, $\gamma_1 = 1, \gamma_2 = 1$, $q = q_0$)

5.4. Influence of elastic foundation coefficients

In this example, the influence of parameters ($\bar{K}_0$, $\bar{J}_0$) on the critical load $\bar{N}$ and the central deflection $\bar{w}$ of the SSSS GPL-FGM microplate with D1 pattern are plotted in Fig. 6. In this investigation, the parameters $\bar{K}_0$ and $\bar{J}_0$ are varied from 0 to 150. From the graphs, it can be observed that as foundation parameters ($\bar{K}_0$, $\bar{J}_0$) increase, the critical load $\bar{N}$ of the microplate increases, while the deflection $\bar{w}$ decreases. For example, when $W_{GPL} = 1.5\%$ with the pattern D1, and for $p = 1$, the critical load $\bar{N}$ of the microplate under biaxial compression increases from 17.2807 at $\bar{K}_0 = 0$, $\bar{J}_0 = 0$ to 31.7129 at $\bar{K}_0 = 150$, $\bar{J}_0 = 150$, corresponding to an increase of 83.52% (Fig. 6(a)). Similarly, the deflection $\bar{w}$ of the microplate reduces from 0.1001 at $\bar{K}_0 = 0$, $\bar{J}_0 = 0$ to 0.0538 at $\bar{K}_0 = 150$, $\bar{J}_0 = 150$, corresponding to a decrease of 46.25% (Fig. 6(b)). This behaviour occurs because the foundation parameters enhance the overall stiffness of the microplate structure.

In addition, the parameter $\bar{J}_0$ has a more pronounced effect on both the critical load $\bar{N}$ and the deflection $\bar{w}$ compared to the parameter $\bar{K}_0$. For example, when $\bar{K}_0 = 0$, the critical load $\bar{N}$ of the microplate under biaxial compression increases from 17.2807 at $\bar{J}_0 = 0$ to 31.0170 at $\bar{J}_0 = 150$, corresponding to an increase of 79.49%, while when $\bar{J}_0 = 0$, the critical load $\bar{N}$ of the microplate under biaxial compression increases from 17.2807 at $\bar{K}_0 = 0$ to 17.9766 at $\bar{K}_0 = 150$, corresponding to an increase of 4.03%. Similarly, when $\bar{K}_0 = 0$, the deflection $\bar{w}$ of the microplate decreases from 0.1001 at $\bar{J}_0 = 0$ to 0.0550 at $\bar{J}_0 = 150$, corresponding to a reduction of 45.05%, while when $\bar{J}_0 = 0$, the deflection $\bar{w}$ of the microplate reduces from 0.1001 at $\bar{K}_0 = 0$ to 0.0961 at $\bar{K}_0 = 150$, corresponding to a reduction of 4.00%. This is because the parameter $\bar{J}_0$ is associated with shear deformation and slope continuity of the structure, whereas the parameter $\bar{K}_0$ only affects the vertical displacement at a point. The shear interaction introduced by the parameter $\bar{J}_0$ effectively creates a "distributed coupling" among neighboring points, which redistributes internal forces and enhances the overall stiffness of the structure more efficiently.

6. Conclusions

In this paper, the semi-analytical solution for the static bending and buckling problems of the microplate placed on the Winkler-Pasternak elastic foundation is presented. The plate model is made of a FGM (Ceramic/metal) reinforced by GPLs. Five GPL patterns, symmetric D1, symmetric D2, asymmetric D3, asymmetric D4, and uniform D5, are evaluated for the microplate. The governing equations and solutions of the microplate model are formulated based on the four-unknown refined plate theory, the modified couple stress theory, and the Ritz method. Parametric studies are then performed; the main findings can be summarized as follows:

- The size-dependent effect has a significant influence on the non-dimensional central deflection $\bar{w}$ and the critical load $\bar{N}$ of the GPL-FGM microplate when the ratio h/l_0 is small. When $h/l_0 > 10$, the influence of the size-dependent effect becomes negligible.

- Increasing the GPL weight fraction enhances the stiffness of the microplate model, resulting in higher critical load $\bar{N}$, while reducing the deflection $\bar{w}$. The GPL weight fraction has a significant impact on the microplate's behaviour.

- The Pasternak foundation parameter $\bar{J}_0$ has a much stronger influence on the deflection $\bar{w}$ and the critical load $\bar{N}$ of the GPL-FGM microplate than the Winkler foundation parameter $\bar{K}_0$.

Note that the present microplate model is developed under several simplified assumptions that introduce certain limitations. The four-unknown refined plate theory and the MCST model employed herein assume small strains, linear elasticity, and a two-dimensional plate formulation; therefore, the through-thickness stress distribution in very thick plates and geometric or material nonlinearities may not be fully captured. The applicability of MCST is governed by the material length-scale parameter, and when the ratio h/l_0 becomes extremely small, the validity of the MCST formulation should be considered with caution. The FGM-GPL material properties are estimated using the power-law homogenization and the modified Halpin–Tsai scheme, which assume an approximately continuous dispersion of GPLs and thus do not reflect microscale heterogeneity or interphase effects. In addition, multi-physics influences (thermal, electrical, moisture, etc.) are not considered in the present analysis. These assumptions and limitations should be considered when applying the present results to real engineering structures, especially those involving materials with complex microstructures. Future research directions may include: (a) developing three-dimensional models for GPL-FGM microplates, and (b) investigating the transient and multi-physics responses of GPL-FGM microplates.

References

[1] Tadigadapa, S., Mateti, K. (2009). Piezoelectric MEMS sensors: state-of-the-art and perspectives. *Measurement Science and Technology*, 20(9):092001.

[2] Hierold, C., Jungen, A., Stampfer, C., Helbling, T. (2007). Nano electromechanical sensors based on carbon nanotubes. *Sensors and Actuators A: Physical*, 136(1):51–61.

[3] Jha, D. K., Kant, T., Singh, R. K. (2013). A critical review of recent research on functionally graded plates. *Composite Structures*, 96:833–849.

[4] Thai, H.-T., Kim, S.-E. (2015). A review of theories for the modeling and analysis of functionally graded plates and shells. *Composite Structures*, 128:70–86.

[5] Ghatage, P. S., Kar, V. R., Sudhagar, P. E. (2020). On the numerical modelling and analysis of multi-directional functionally graded composite structures: A review. *Composite Structures*, 236:111837.

[6] Roun, S., Nguyen, V.-L., Rungamornrat, J. (2024). Free Vibration and Buckling Analyses of Functionally Graded Plates with Graphene Platelets Reinforcement. *Journal of Computing and Information Science in Engineering*, 25(1):011002.

[7] Nguyen, V.-L., Nguyen, V.-L., Tran, M.-T., Dang, X.-T. (2024). Investigation of static buckling and bending of nanoplates made of new functionally graded materials considering surface effects on an elastic foundation. *Acta Mechanica*, 235(12):7807–7833.

[8] Chu, T.-B., Nguyen, V.-L., Tran, M.-T., Nguyen, V.-L., Dang, X.-T. (2025). Free Vibration Analysis of Graphene-Reinforced FGM Nanoplates with Surface Energy Effects Resting on Elastic Foundation. *Iranian Journal of Science and Technology, Transactions of Mechanical Engineering*, 49(1):235–256.

[9] Eringen, A. C. (1972). Nonlocal polar elastic continua. *International Journal of Engineering Science*, 10 (1):1–16.

[10] Eringen, A. C. (1983). On differential equations of nonlocal elasticity and solutions of screw dislocation and surface waves. *Journal of Applied Physics*, 54(9):4703–4710.

[11] Mindlin, R. D. (1965). Second gradient of strain and surface-tension in linear elasticity. *International Journal of Solids and Structures*, 1(4):417–438.

[12] Aifantis, E. C. (1999). Strain gradient interpretation of size effects. *International Journal of Fracture*, 95 (1–4):299–314.

[13] Lim, C. W., Zhang, G., Reddy, J. N. (2015). A higher-order nonlocal elasticity and strain gradient theory and its applications in wave propagation. *Journal of the Mechanics and Physics of Solids*, 78:298–313.

[14] Ghayesh, M. H., Farajpour, A. (2019). A review on the mechanics of functionally graded nanoscale and microscale structures. *International Journal of Engineering Science*, 137:8–36.

[15] Pham, Q.-H., Tran, T. T., Nguyen, P.-C. (2023). Nonlocal free vibration of functionally graded porous nanoplates using higher-order isogeometric analysis and ANN prediction. *Alexandria Engineering Journal*, 66:651–667.

[16] Banh-Thien, T., Dang-Trung, H., Le-Anh, L., Ho-Huu, V., Nguyen-Thoi, T. (2017). Buckling analysis of non-uniform thickness nanoplates in an elastic medium using the isogeometric analysis. *Composite Structures*, 162:182–193.

[17] Phung-Van, P., Thai, C. H., Nguyen-Xuan, H., Abdel-Wahab, M. (2019). An isogeometric approach of static and free vibration analyses for porous FG nanoplates. *European Journal of Mechanics - A/Solids*, 78:103851.

[18] Dang, X.-T., Nguyen, V.-L., Tran, M.-T., Nguyen-Thi, B.-P., Le, T.-T. (2025). Buckling and bending analysis of FGP nanoplates resting on Pasternak foundation considering non-local and surface effects simultaneously using pb2-Ritz method. *Composite Structures*, 359:118971.

[19] Yang, F., Chong, A., Lam, D., Tong, P. (2002). Couple stress based strain gradient theory for elasticity. *International Journal of Solids and Structures*, 39(10):2731–2743.

[20] Xia, W., Wang, L., Yin, L. (2010). Nonlinear non-classical microscale beams: Static bending, postbuckling and free vibration. *International Journal of Engineering Science*, 48(12):2044–2053.

[21] Reddy, J. N., Berry, J. (2012). Nonlinear theories of axisymmetric bending of functionally graded circular plates with modified couple stress. *Composite Structures*, 94(12):3664–3668.

[22] Lien, T. V., Ha, L. T. (2024). Vibration analysis of Timoshenko microbeams made of functionally graded materials on a Winkler-Pasternak elastic foundation. *Vietnam Journal of Mechanics*, 46(1):31–43.

[23] Liu, S., Yu, T., Bui, T. Q. (2017). Size effects of functionally graded moderately thick microplates: A novel non-classical simple-FSDT isogeometric analysis. *European Journal of Mechanics - A/Solids*, 66: 446–458.

[24] Binh, C. T. (2025). Buckling analysis of GPL-reinforced FGM microplates using Pb-2 Ritz functions. *Journal of Science and Technology in Civil Engineering (JSTCE) - HUCE*, 19(2):119–132.

[25] Nguyen, V.-L., Chu, T.-B. (2024). Free vibration analysis of graphene-reinforced FGM microplates under different boundary conditions. *Journal of Science and Technology - The University of Danang*, 22(11B): 70–76.

[26] Chen, D., Yang, J., Kitipornchai, S. (2019). Buckling and bending analyses of a novel functionally graded porous plate using Chebyshev-Ritz method. *Archives of Civil and Mechanical Engineering*, 19 (1):157–170.

[27] Jing, Z., Liu, Y., Duan, L., Wang, S. (2025). Three-dimensional buckling analysis of stiffened plates with complex geometries using energy element method. *International Journal of Solids and Structures*, 306: 113105.

[28] Akgöz, B., Civalek, O. (2022). Buckling Analysis of Functionally Graded Tapered Microbeams via Rayleigh–Ritz Method. *Mathematics*, 10(23):4429.

[29] Zhao, S., Zhao, Z., Yang, Z., Ke, L., Kitipornchai, S., Yang, J. (2020). Functionally graded graphene reinforced composite structures: A review. *Engineering Structures*, 210:110339.

[30] Nguyen, V.-L., Limkatanyu, S., Thai, H.-T., Rungamornrat, J. (2024). Simple First-order Shear Deformation Theory for Free Vibration of FGP-GPLRC Spherical Shell Segments. *Mechanics of Advanced Materials and Structures*, 31(25):6944–6961.

[31] Tran, H.-Q., Vu, V.-T., Tran, M.-T. (2023). Free vibration analysis of piezoelectric functionally graded porous plates with graphene platelets reinforcement by pb-2 Ritz method. *Composite Structures*, 305: 116535.

[32] Thai, H.-T., Kim, S.-E. (2013). A size-dependent functionally graded Reddy plate model based on a modified couple stress theory. *Composites Part B: Engineering*, 45(1):1636–1645.

[33] Yang, J., Chen, D., Kitipornchai, S. (2018). Buckling and free vibration analyses of functionally graded graphene reinforced porous nanocomposite plates based on Chebyshev-Ritz method. *Composite Structures*, 193:281–294.

[34] Nguyen, V.-L., Nguyen, V.-L., Nguyen, T.-A., Tran, M.-T. (2024). Dynamic responses of saturated functionally graded porous plates resting on elastic foundation and subjected to a moving mass using pb2-Ritz method. *Acta Mechanica*, 235(8):5301–5327.

[35] Nguyen, V.-L., Sukulthanasorn, N., Smittakorn, W., Rungamornrat, J. (2025). Electro-thermal vibration of graphene platelets reinforced functionally graded piezoelectric microplates under different boundary conditions. *International Journal of Solids and Structures*, 314:113273.

[36] Arefi, M., Mohammad-Rezaei Bidgoli, E., Dimitri, R., Tornabene, F. (2018). Free vibrations of functionally graded polymer composite nanoplates reinforced with graphene nanoplatelets. *Aerospace Science and Technology*, 81:108–117.

[37] Thai, H.-T., Choi, D.-H. (2013). Size-dependent functionally graded Kirchhoff and Mindlin plate models based on a modified couple stress theory. *Composite Structures*, 95:142–153.

[38] Abazid, M. A., Sobhy, M. (2018). Thermo-electro-mechanical bending of FG piezoelectric microplates on Pasternak foundation based on a four-variable plate model and the modified couple stress theory. *Microsystem Technologies*, 24(2):1227–1245.

[39] Van Hieu, D., Hoa, N. T., Chan, D. Q. (2023). Size-Dependent Mechanical Analysis of Imperfect FG Mindlin Microplate with Porosities Resting on Elastic Foundation Through the Modified Couple Stress Theory. *Iranian Journal of Science and Technology, Transactions of Mechanical Engineering*, 47(1): 163–185.

[40] Nguyen, P.-C., Pham, Q.-H. (2023). A nonlocal isogeometric model for buckling and dynamic instability analyses of FG graphene platelets-reinforced nanoplates. *Materials Today Communications*, 34:105211.

Appendix A.

The stress resultants ($N_{xx}, N_{yy}, N_{xy}, M^b_{xx}, M^b_{yy}, M^b_{xy}, M^s_{xx}, M^s_{yy}, M^s_{xy}, Q_{xz}, Q_{yz}$) and ($P_{xx}, P_{yy}, P_{xy}, P_{yz}, P_{xz}, R_{xx}, R_{yy}, R_{xy}, S_{yz}, S_{xz}$) can be determined by:

$$\begin{cases} N_{xx} = A_{11}\varepsilon^0_{xx} + A_{12}\varepsilon^0_{yy} + B_{11}k^b_{xx} + B_{12}k^b_{yy} + C_{11}k^s_{xx} + C_{12}k^s_{yy} \\ N_{yy} = A_{12}\varepsilon^0_{xx} + A_{22}\varepsilon^0_{yy} + B_{12}k^b_{xx} + B_{22}k^b_{yy} + C_{12}k^s_{xx} + C_{22}k^s_{yy} \\ N_{xy} = A_{66}\gamma^0_{xy} + B_{66}k^b_{xy} + C_{66}k^s_{xy} \end{cases} \tag{A.1}$$

$$\begin{cases} M^b_{xx} = B_{11}\varepsilon^0_{xx} + B_{12}\varepsilon^0_{yy} + D_{11}k^b_{xx} + D_{12}k^b_{yy} + F_{11}k^s_{xx} + F_{12}k^s_{yy} \\ M^b_{yy} = B_{12}\varepsilon^0_{xx} + B_{22}\varepsilon^0_{yy} + D_{12}k^b_{xx} + D_{22}k^b_{yy} + F_{12}k^s_{xx} + F_{22}k^s_{yy} \\ M^b_{xy} = B_{66}\gamma^0_{xy} + D_{66}k^b_{xy} + F_{66}k^s_{xy} \end{cases} \tag{A.2}$$

$$\begin{cases} M^s_{xx} = C_{11}\varepsilon^0_{xx} + C_{12}\varepsilon^0_{yy} + F_{11}k^b_{xx} + F_{12}k^b_{yy} + G_{11}k^s_{xx} + G_{12}k^s_{yy} \\ M^s_{yy} = C_{12}\varepsilon^0_{xx} + C_{22}\varepsilon^0_{yy} + F_{12}k^b_{xx} + F_{22}k^b_{yy} + G_{12}k^s_{xx} + G_{22}k^s_{yy} \\ M^s_{xy} = C_{66}\gamma^0_{xy} + F_{66}k^b_{xy} + G_{66}k^s_{xy} \end{cases} \tag{A.3}$$

$$\begin{cases} \left(P_{xx}, P_{yy}, P_{xy}\right) = \tilde{A}_n \left(\chi^0_{xx}, \chi^0_{yy}, \chi^0_{xy}\right) + \tilde{B}_n \left(\chi^1_{xx}, \chi^1_{yy}, \chi^1_{xy}\right) \\ \left(P_{yz}, P_{xz}\right) = \tilde{A}_n \left(\chi^0_{yz}, \chi^0_{xz}\right) + \tilde{C}_n \left(\chi^1_{yz}, \chi^1_{xz}\right) \end{cases} \tag{A.4}$$

$$\begin{cases} \left(R_{xx}, R_{yy}, R_{xy}\right) = \tilde{B}_n \left(\chi^0_{xx}, \chi^0_{yy}, \chi^0_{xy}\right) + \tilde{D}_n \left(\chi^1_{xx}, \chi^1_{yy}, \chi^1_{xy}\right) \\ \left(S_{yz}, S_{xz}\right) = \tilde{C}_n \left(\chi^0_{yz}, \chi^0_{xz}\right) + \tilde{G}_n \left(\chi^1_{yz}, \chi^1_{xz}\right) \end{cases} \tag{A.5}$$

$$\begin{cases} Q_{yz} = A^s_{44} \gamma^s_{yz} \\ Q_{xz} = A^s_{55} \gamma^s_{xz} \end{cases} \tag{A.6}$$

in which $\left(A_{ij}, B_{ij}, D_{ij}, C_{ij}, F_{ij}, G_{ij}, A^s_{ij}\right)$ and $(\tilde{A}_n, \tilde{B}_n, \tilde{D}_n, \tilde{C}_n, \tilde{G}_n)$ are given by

$$\begin{aligned} &\left(A_{ij}, B_{ij}, D_{ij}, C_{ij}, F_{ij}, G_{ij}\right) = \int_{-h/2}^{h/2} \left(1, z, z^2, f, zf, f^2\right) \bar{C}_{ij} dz, \quad (ij = 11, 12, 22, 66) \\ &A^s_{ij} = \int_{-h/2}^{h/2} g(z)^2 \bar{C}_{ij} dz, \quad (ij = 44, 55) \end{aligned} \tag{A.7}$$

$$(\tilde{A}_n, \tilde{B}_n, \tilde{D}_n, \tilde{C}_n, \tilde{G}_n) = \int_{-h/2}^{h/2} 2G_c l_0^2 \left\{1, (1 + f_{,z}), (1 + f_{,z})^2, f_{,zz}, f^2_{,zz}\right\} dz \tag{A.8}$$